

# We are IntechOpen, the world's leading publisher of Open Access books Built by scientists, for scientists

6,900

Open access books available

185,000

International authors and editors

200M

Downloads

Our authors are among the

154

Countries delivered to

TOP 1%

most cited scientists

12.2%

Contributors from top 500 universities



WEB OF SCIENCE™

Selection of our books indexed in the Book Citation Index  
in Web of Science™ Core Collection (BKCI)

Interested in publishing with us?  
Contact [book.department@intechopen.com](mailto:book.department@intechopen.com)

Numbers displayed above are based on latest data collected.  
For more information visit [www.intechopen.com](http://www.intechopen.com)



# Polarization-Sensitive Optical Coherence Tomography in Cardiology

Wen-Chuan Kuo

*Institute of Electro-optical Science and Technology, National Taiwan Normal University  
Taiwan*

## 1. Introduction

Atherosclerotic vascular disease is a common cause of morbidity and mortality in developed countries (Arroyo & Lee, 1999). In particular, the rupture of atherosclerotic plaques is the most common event initiating acute ischemic heart disease (Shah, 2003). Therefore, it is crucial to detect vulnerable coronary atheromatous plaques prior to their rupture or erosion to prevent irreversible myocardial damage. Autopsy studies have identified several histological characteristics of these vulnerable plaques, such as a large lipid pool, thin fibrous cap (<65  $\mu\text{m}$ ), and activated macrophages near the fibrous cap (Falk et al., 1995). Therefore, modalities capable of visualizing the vessel wall might help in detecting lesions with high risks for acute events (Pasterkamp et al., 2000; Peters et al., 1994). There are several plaque imaging modalities. The oldest and most widely used technology is X-ray angiography, which can detect narrowing of the coronary blood vessels. The first imaging technique to demonstrate the benefits of imaging inside the arterial wall is intravascular ultrasound (IVUS). However, the current resolution is not sufficient to visualize the thin fibrous caps and small disruptions within the intimal and medial dissections. In the 1980s, coronary angiography, which allows direct visualization of the surface color and superficial morphology of atherosclerotic plaque, thrombus, neointima, and stent struts, was introduced. However, it cannot help in the assessment of subsurface lesions. Other proposed techniques include electron beam computed tomography (EBCT), magnetic resonance imaging (MRI), or positron emission tomography (PET); these are noninvasive screening tools that do not subject the patient to catheterization. In addition to the aforementioned techniques, which are merely a selection of the imaging modalities currently used *in vivo* or that are in the validation stage, the use of optical techniques for biomedical imaging is gaining considerable attention. This is largely due to the potential of optical techniques to provide high-resolution imaging without the need for ionizing radiation and associated risks.

Optical coherence tomography (OCT), which is based on a low-coherence interferometer, has emerged as a rapid, non-contact and noninvasive, high-resolution imaging tool (Huang et al., 1991). From the mid-1990s, the ability of intravascular OCT to provide high-resolution (10–20  $\mu\text{m}$ ) cross-sectional images of both *in vitro* human aorta and coronary arteries has been demonstrated (Brezinski et al., 1996; Fujimoto et al., 1995). The resolution of OCT images was up to 10 times better than that of conventional ultrasound, MRI, and computed tomography (CT) (Jang et al., 2002; Yabushita et al., 2002). Therefore, using OCT, small

Source: *Advances in Lasers and Electro Optics*, Book edited by: Nelson Costa and Adolfo Cartaxo, ISBN 978-953-307-088-9, pp. 838, April 2010, INTECH, Croatia, downloaded from SCIYO.COM

structural details (such as the width of intimal caps and the presence of fissures in atherosclerotic plaques (Bresinski et al., 1997) could be resolved and intramural collections of lipid within the intima of a vessel wall could be detected (Brezinski et al., 1996; Fujimoto et al., 1995). Furthermore, the objective OCT image criterion for risk-stratifying plaque characterization has been established on the basis of the intrinsic optical properties of a typical plaque, whose constituents are lipid, calcium, and fibrous tissue (Bresinski et al., 1997; Jang et al., 2002; Stamper et al., 2006; Tearney et al., 2006; Yabushita et al., 2002). On this basis, OCT has a detection sensitivity and specificity of 71%–79% and 97%–98% for fibrous plaques, 95%–96% and 97% for fibrocalcific plaques, and 90%–94% and 90%–92% for lipid-rich plaques, respectively (Tearney et al., 2006; Yabushita et al., 2002). Moreover, OCT has also been shown to quantify plaque macrophage content (Tearney et al., 2003) in lipid-rich plaques and to assess the success of intracoronary stent implantation in patients with coronary artery disease during percutaneous intra-arterial procedures (Bouma et al., 2003). At present, a company, LightLab Imaging, is targeting the cardiovascular market using commercializing intravascular OCT technology by providing dedicated imaging wires and occlusion balloon catheters.

In general, OCT images are obtained from measurements of the echo time delay and the intensity of the backscattered light from a specimen. Further, OCT employs the inherent differences in the index of refraction, rather than enhancement with dyes, to differentiate tissue types. However, since the plaque components are heterogeneous, they may sometimes generate reflected signals that confuse or obscure the identity of these components; multiple scattering by the cap also creates difficulties in identifying the plaque due to the diffuse nature of the plaque border (Stamper et al., 2006). Polarization-sensitive OCT (PS-OCT), a functional mode of OCT, combines the advantages of OCT with additional image contrasts obtained by using the birefringence of the specimen as a contrast agent. Many biological tissues have a microscopic fibrous structure and so exhibit intrinsic birefringence. Moreover, changes in birefringence may indicate changes in functionality, structure, or viability of tissues in the early stages of the disease (de Boer et al., 1997).

From 2004, we have been presenting the application of PS-OCT in human atherosclerosis, and have proposed approaches to characterize a plaque lesion on the basis of its birefringence property (Kuo et al., 2004; 2005; 2007). Moreover, in a recent study, our laboratory has assessed the arterial characteristics in human atherosclerosis by quantitatively determining both scattering and birefringence properties of vessel tissue from PS-OCT images (Kuo et al., 2007; 2008). Based on our findings, a quantitative PS-OCT image criterion for plaque characterization was constructed. In the remainder of this chapter, the results that we obtained using the PS-OCT system for imaging human atherosclerosis *in vitro* are summarized. We hope that our results, along with the results from other investigators, will construe a step forward in the application of PS-OCT imaging technology for clinically diagnosing atherosclerosis in the near future.

## **2. Principle of polarization-sensitive optical coherence tomography (PS-OCT) system**

The optical setup of the PS-OCT system used in this study is shown in Fig. 1. A collimated beam from a superluminescent diode (SLD) centered at a wavelength of 837 nm with a spectral bandwidth of 17.5 nm was used as a low-coherence light source in a Michelson interferometer. The axial resolution, which depends on the temporal coherence properties of

the SLD), was  $17\ \mu\text{m}$ , while the lateral resolution (determined by the numerical aperture of the objective) was  $10\ \mu\text{m}$ . The incident beam was vertically polarized by a polarizer placed in the interferometer. A nonpolarization beam splitter (BS) was used to split the light wave into signal and reference beams. In the Michelson interferometer, a quarter-wave plate (QWP) with an azimuth angle set at  $45^\circ$  to the horizontal was used to focus the circular polarized light onto the examined specimen. On the other hand, the reference beam light was directed to a plane mirror mounted on a linear translator, which repetitively scanned the reference arm optical path length at a constant speed ( $1\ \text{mm/s}$ ). Another QWP (set at  $22.5^\circ$  to the horizontal) in the reference beam path rotated the polarization of the incident laser beam by  $45^\circ$ , thereby becoming the reflected reference beam.

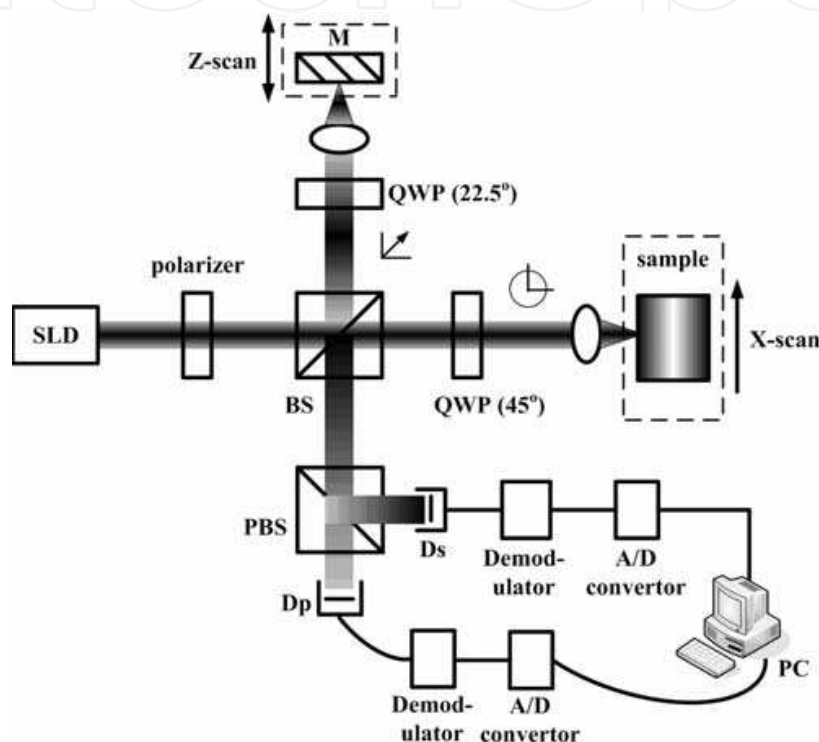


Fig. 1. Schematic of the conventional PS-OCT system: SLD, superluminescent diode; QWP, quarter wave plate; M, reference mirror; BS: beam splitter; PBS, polarized beam splitter; Dp and Ds, photo-detectors; PC, personal computer.

The laser beam was reflected from the specimen and recombined with the reflected reference beam, and then both the horizontal ( $P$  wave) and vertical components ( $S$  wave) were independently directed toward two photodetectors  $Dp$  and  $Ds$ , respectively, using a polarized BS (PBS). From the ac coupling of the detector signals, the full interferometric signals were recorded. The amplitudes  $A_i(z)$  and phases  $\phi_i(z)$  of the interference signals at different depths ( $z$ ) were determined using the Hilbert transform;  $i = P$  and  $S$  represent the  $P$  and  $S$  polarization states, respectively. Three parameters—the backscatter intensity  $R(z)$ , phase retardation  $\Phi(z)$ , and fast-axis angle  $\beta(z)$  of a specimen—were calculated using the amplitude and phase of the interference signal (Hitzenberger et al., 2001):

$$R(z) \sim A_p(z)^2 + A_s(z)^2 \quad (1)$$

$$\Phi(z) = \tan^{-1}(A_s(z)/A_p(z)) \quad (2)$$

$$\beta(z) = 1/2 \times (180^\circ - \Delta\phi) \quad (3)$$

Here,  $\Delta\phi = \phi_p - \phi_s$  is the phase difference between the P- and S-polarized heterodyne signals. Finally, 2D images of the above three parameters were obtained simultaneously by using repeated A-scan acquisition and mechanically scanning the specimens laterally through a focused 0.5 mW signal beam. In this experiment, the system sensitivity was obtained as 100 dB using a highly reflective plane mirror as the test object in this setup. The following section demonstrates our preliminary *in vitro* investigations of human aortic specimens using PS-OCT.

In this study, we adapted a free-space PS-OCT system to precisely control the polarization state of the laser beam used in birefringent imaging. Several other groups have developed a high speed fiber-based PS-OCT system for application as a medical instrument *in vivo* (Guo et al., 2004; Park et al., 2001; 2004; Saxer et al., 2000). Moreover, an optically clear hemoglobin-based blood substitute has also been used to displace blood and enable OCT imaging with minimal patient discomfort (Villard et al., 2002). Further, several Fourier domain PS-OCT techniques (Park et al., 2005; Yamanari et al., 2006; Zhang et al., 2004) have been reported recently and have received considerable attention due to the high data acquisition rates (e.g., acquisition at 80 to 110 fps), which can eliminate motion artifacts and reduce ischemia during blood-free optical imaging. This allows for comprehensive scanning of long arterial segments during a short balloon occlusion or even 1 bolus liquid flush without occlusion. The first clinical study using this technology is being initiated in order to investigate vulnerable plaque hypothesis in a prospective multicenter manner. By combining the above features, PS-OCT can be used to measure reflected intensity, phase retardation, and fast-axis angle distributions, and thereby provide a greater contrast than is available with conventional OCT systems.

### 3. In vitro PS-OCT imaging of human atherosclerosis

Specimens of the aorta with white or yellow plaque were obtained from heart transplant recipients at the National Taiwan University Hospital, Taiwan. The photographs of some specimens are shown in Fig. 2. The protocol was approved by the ethics committees of the National Taiwan University Hospital. The specimens were dipped in saline (4°C), cut into segments smaller than 1 × 1 cm, and examined. Each segment was mounted in a cuvette and moistened with a normal saline bath maintained at 37°C during the imaging. Only the intimal surface was exposed for PS-OCT imaging. The aortic specimen regions imaged with PS-OCT were marked for subsequent histopathological examination. After PS-OCT imaging, all the specimens were fixed in 10% neutral formalin for 24 h and then processed for standard paraffin embedding. Serial sections with 4 μm thickness were cut within the region of the PS-OCT examination, and stained with hematoxylin and eosin (H and E) for routine examination. The distribution of the collagen structure in the plaque lesion was also examined using Masson trichrome and picrosirius red staining procedures as well as a polarization microscope. Finally, the entire specimens were classified into normal vessel (N), lipid (L), fibrocalcific (C), and fibrous lesions (F) by a pathologist (J. J. Shyu).

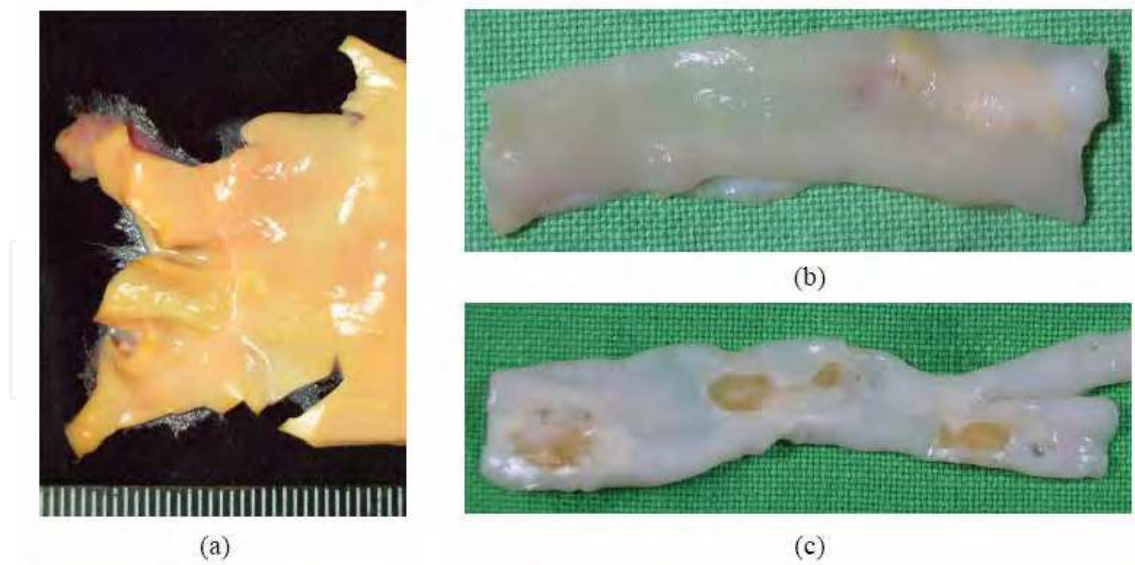


Fig. 2. Photographs of the aorta with white or yellow plaque.

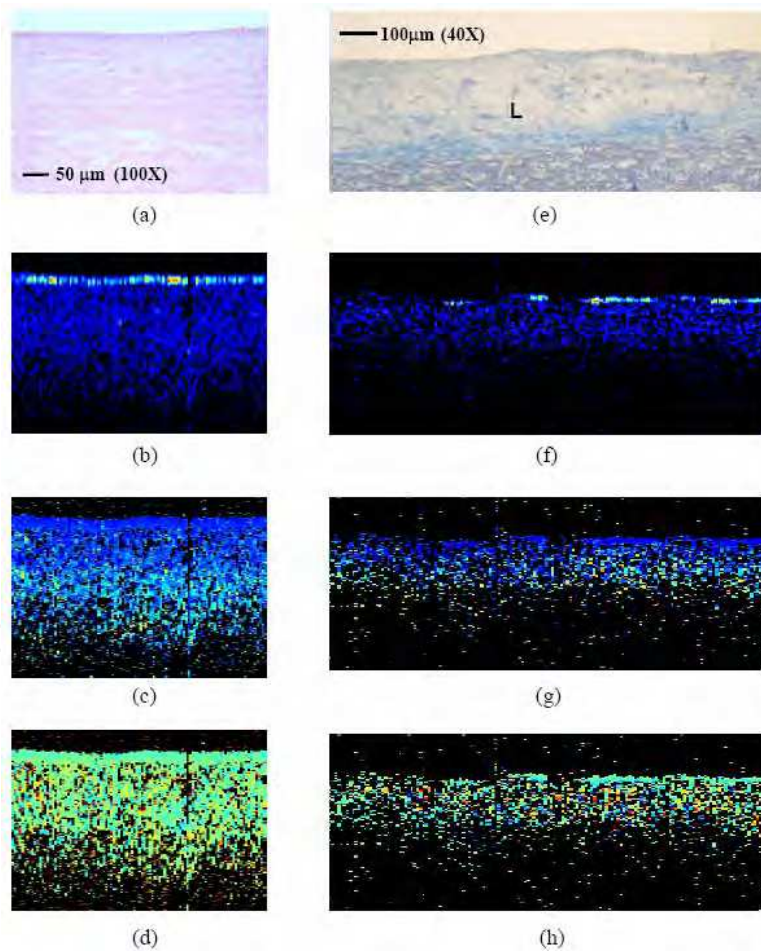


Fig. 3. Histological and PS-OCT images of a normal aortic wall (left column) and a plaque with lipid-loaded lesion (right column): (a) Histology (H and E; magnification  $\times 100$ ); (e) Histology (Masson's trichrome; magnification  $\times 40$ ); (b), (f) Back-scattered intensity image; (c), (g) Phase retardation image (linear color scale degrees); (d), (h) Fast-axis angle image (linear color scale degrees).

The PS-OCT images of representative specimens are shown in Figs. 3–6. The histological image of the normal vessel wall [Fig. 3(a)] showing a medial layer below the intima is compared with the PS-OCT image of the same specimen [Fig. 3(b)]. The signal-rich layer closest to the lumen is the intima. In the normal vessel wall, the phase retardation increases uniformly [Fig. 3(c)], and the pseudocolor distribution of the fast-axis angle signals is also uniform [Fig. 3(d)]. The pale area in Fig. 3(e) is a subintimal lipid-loaded region (L), which is morphologically composed mostly of the necrotic debris of foamy cells. Because of the paraffin embedding process, the solvent treatment removes the lipid from these lipid-loaded structures, which therefore appear as empty spaces in stained sections [Fig. 3(e)]. The corresponding PS-OCT image [Fig. 3(f)] reveals a decreased signal density under a thin homogeneous surface band. Moreover, the phase retardation and fast-axis angle signals are distributed in a slightly more random manner in the atherosclerotic lesion [Figs. 3(g) and 3(h), respectively] than in a normal vessel wall [Figs. 3(c) and 3(d)].

Moreover, the PS-OCT and histological images showed a plaque having small amounts of fibrous connective tissue (blue stain; black arrows) within a lipid-loaded area [Fig. 4(a)]. The signal density (arrows) was stronger, the backscattering signal was more heterogeneous [Fig. 4(b)], and the variation in the phase retardation [Fig. 4(c)] and fast-axis angle distribution [Fig. 4(d)] was more abrupt in the fibrous tissue than in the lipid-loaded region (L). Figure 4(e) shows a typically advanced plaque within the vascular intima; it is characterized by a necrotic lipid core covered by a thicker fibrous cap (CF ~250  $\mu\text{m}$ ; stained blue with Masson's trichrome). Plaque development in the vascular wall involves a reorganization of intimal collagen fibers (Rekhter, 1999). Figure 4(f) shows a relatively deep

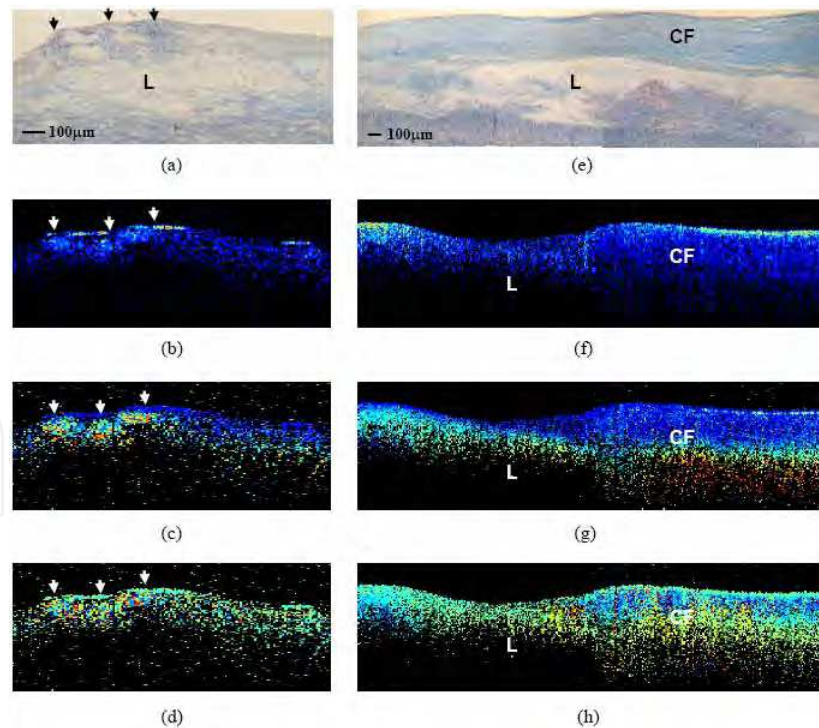


Fig. 4. Histological and PS-OCT images of vessel wall with a small fibrous lesion in the lipid-loaded area (left column) and a lipid-loaded fibroatheroma with a thick fibrous cap (right column): (a), (e) Histology (Masson's Trichrome;  $\times 40$ ); (b), (f) Back-scattered intensity image; (c), (g) Phase retardation image (linear color scale degrees); (d), (h) Fast-axis angle image (linear color scale degrees).

lipid-loaded (*L*) area close to the media. The medial layer had a low backscattering intensity, and hence, the interface between the plaque and the media was not well defined. A comparison of the PS-OCT [Figs. 4(g) and 4(h)] images with the histological images [Figs. 4(e)] showed gradual changes in phase retardation and fast-axis angle signals, which were due to the accumulation of collagen fiber in the plaque. Further, the changes in the pseudocolor in Fig. 4(g) were more uniform within the vessel wall than in those regions indicated by the arrows in Fig. 4(c).

Fig. 5 also shows an atheroma plaque (\*) of a coronary artery stained with trichrome (a, 40 $\times$ ) and picosirius red (b, 100 $\times$ ), which was examined under a polarization microscope (c, 100 $\times$ ). The structure above the mark (\*) is the fibrous cap in the tunica intima, and the structure below the mark (\*) is the tunica media. Picosirius polarized microscopy reveals birefringence regions (e.g., organized collagen in a vessel wall). The intense birefringence of the collagen fiber represented in Fig. 5(e), left region, is confirmed by Figure 5(c) wherein the thick collagen fiber can be observed (in orange color). The fine collagen fiber (green color) of Fig. 5(c) is also consistent with small changes in the phase retardation shown in the right region of Fig. 5(e).

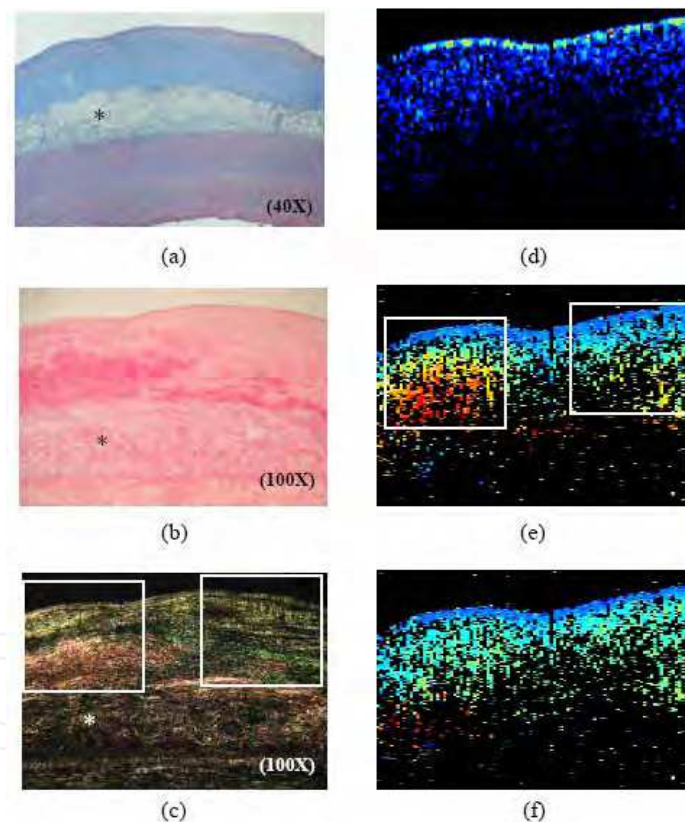


Fig. 5. Lipid-loaded fibroatheroma with a thick fibrous cap. (a) Histology (Masson's trichrome;  $\times 40$ ); (b) histology and (c) examined under polarization microscope (Picosirius polarization;  $\times 40$ ); (d) back-scattered intensity image; (e) phase retardation image (linear color scale degrees); (f) fast-axis angle (linear color scale degrees).

Finally, two fibrocalcific plaques are shown in Fig. 6. The PS-OCT image showed a large sharply delineated, signal-rich area of heterogeneous backscattering [Fig. 6(b) and 6(f)], as well as strong birefringence [Fig. 6(c) and 6(g)]. Different structural orientations were also indicated by the PS-OCT image [i.e., different orientations of a fast-axis angle signal in three

parts of the tomogram; see Fig. 6(h)] but not by the H and E stained specimen [Fig. 6(e)]. Since the calcified lesion was damaged during the sectioning process, only a large empty hole with a few calcified fragments appeared within the calcified plaque.

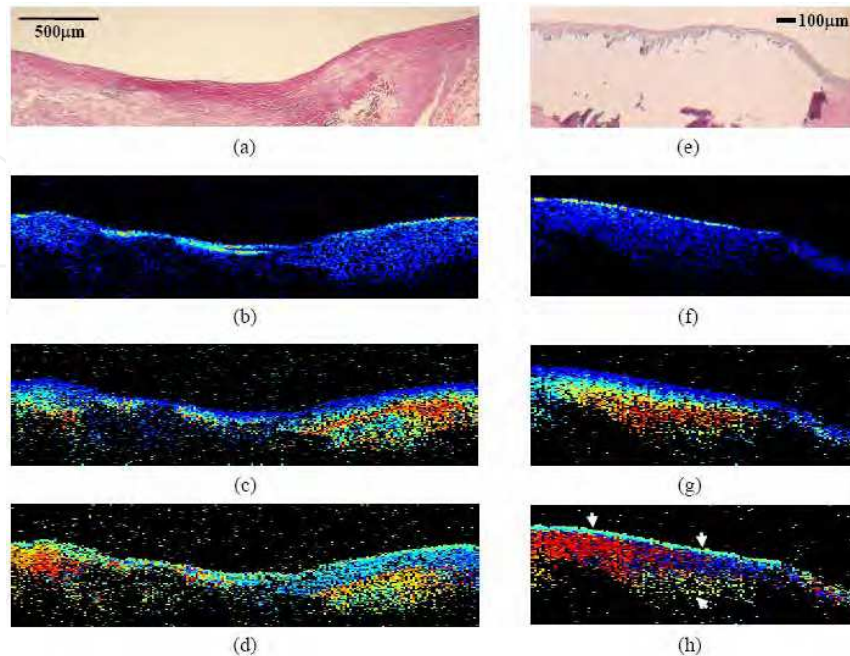


Fig. 6. Histological and PS-OCT images of fibrocalcific plaques: (a), (e) Histology (H and E); (b), (f) Back-scattered intensity image; (c), (g) Phase retardation image (linear color scale degrees); (d), (h) Fast-axis angle image (linear color scale degrees).

Using the above experiments, the capability of PS-OCT for imaging atherosclerotic plaques in human specimens has been evaluated. We have demonstrated that the normal vascular intima has a low intrinsic birefringence property, while changes in birefringence characteristics were apparent in fibrous and calcified plaques; moreover, the birefringence characteristics were different from those in normal vessels and lipid-loaded lesions. By using picosirius staining along with polarization microscopy, we could also identify the thickness of collagen fiber. Recently, the identification of organized collagen fiber in arteries has also been demonstrated by using a single-detector PS-OCT (Giattina et al., 2006). In addition, another report showed that the PS-OCT measurements of birefringence have a strong positive correlation with thick collagen fiber content ( $r = 0.76$ ,  $p < 0.001$ ) and also a smooth muscle cells density ( $r = 0.74$ ,  $p < 0.01$ ) (Nadkarni et al., 2007).

#### 4. Extracting optical properties from PS-OCT images

It is well known that optical properties can be used to indicate whether a tissue is in a normal or pathological state (Kortum & Muraca, 1996). Further, accurate knowledge of optical properties is essential for the optimum use of light in diagnosis and the treatment of diseases. In this study, we constructed a quantitative PS-OCT image criterion for plaque characterization. Following PS-OCT imaging, an algorithm was used to determine both scattering (i.e.,  $\mu_s$  and  $g_{eff}$ ) and birefringence properties (i.e.  $\Delta n$  and  $\beta$ ) of vessel tissue from the above PS-OCT images. The  $\mu_s$  can be thought of as the reciprocal of the average distance a photon travels between scattering events. The  $g_{eff}$  factor describes how isotropic or

anisotropic the scattering is, and is related to the particle size in the specimen. The  $\Delta n$  value characterizes the differential speed of propagation between two orthogonal polarized states of light in the specimen; it may change with derangement and mechanical failure of the collagen network in the vessel. And the  $\beta$  value could be thought of as a parameter of the fiber orientation in fibrous tissues where birefringence is caused by form birefringence.

First, the user selected regions (such as the white rectangle shown in the left column of Fig. 7) corresponding to those evaluated by histopathology. The regions were then automatically divided into several regions of interest (ROIs) (e.g., green dashed inset in the left column of Fig. 7) beginning from the intimal surface and including approximately 25 A-scans. Further, the size of each ROI was kept constant. The  $R$ ,  $\Phi$ , and  $\beta$  signals within each ROI were laterally (i.e., along the x-axis) delineated and averaged. Subsequently,  $\mu_s$  and the root-mean-square scattering angle ( $\theta_{rms}$ ), which can be used to calculate the effective anisotropy factor ( $g_{eff} = \cos(\theta_{rms})$ ), were extracted by fitting the reflectivity signals as a function of depth to an extended Huygens-Fresnel model (Kuo et al., 2008; Levitz et al., 2004; Thrane et al., 2000). This is shown in the right column of Fig. 7.

$$\langle i^2(z) \rangle = \left\{ \frac{\alpha^2 P_R P_S \sigma_b}{\pi \omega_H^2} \right\} \cdot \left\{ \exp(-2\mu_s z) + \frac{4 \exp(-\mu_s z) [1 - \exp(-\mu_s z)]}{1 + \omega_S^2 / \omega_H^2} + [1 - \exp(-\mu_s z)]^2 \frac{\omega_H^2}{\omega_S^2} \right\} \quad (4)$$

Here  $\langle i^2(z) \rangle$  is the mean square of the heterodyne signal current;  $\alpha$ , the power to current conversion ratio;  $P_R$  and  $P_S$ , the power of the reference and input sample beams;  $\sigma_b$ , the effective backscattering cross-section; and  $\omega_H$  and  $\omega_S$ , the  $1/e$  irradiance radius at the probing depth in the absence and presence of scattering, respectively. The pixels near the interface, which was due to the specular reflection between the scattering and non-scattering media, were excluded from the fit (Levitz et al., 2004). Furthermore, the profiles of the averaged phase retardation signals have three layers (black arrows in the right column of Fig. 7).  $\Delta n$  can be calculated by linear least-squares fitting through the averaged  $\Phi$  data over the depth of the ROI, and then its slope can be determined from the formula:

$$\Phi = (360/2\pi) \cdot k_0 \cdot d \cdot \Delta n \quad (5)$$

Here  $k_0$  is the wave vector and  $d$  is the thickness of the fitting range. In addition, the mean fast-axis angle calculated by averaging across the width of the ROI at each depth can be determined from Equation (3).

Statistical analyses were performed using SPSS (version 14.0; SPSS Inc.). A p-value < 0.05 was considered to be statistically significant. The test of significant difference of optical parameters was performed by Kruskal-Wallis statistics and used to evaluate whether the four optical properties contributed to the differentiation between different kinds of vessels. After performing a significant test, multiple comparison procedures were then used to determine which means are different. The following equation was used:

$$|R_i - R_j| > Z_{\alpha/k(k-1)} \times \sqrt{\frac{n_t(n_t+1)}{12}} \times \left( \frac{1}{n_i} + \frac{1}{n_j} \right) \quad (6)$$

Here  $R_i$  is the mean rank of the  $i$  th group;  $R_j$ , the mean rank of the  $j$  th group;  $k$ , the number of independent variables;  $n_t$ , the total number of samples;  $n_i$  and  $n_j$ , the sample numbers of the  $i$  th and  $j$  th group, respectively;  $Z_{\alpha/k(k-1)}$ , the critical value at the significance level  $\alpha$ ; and

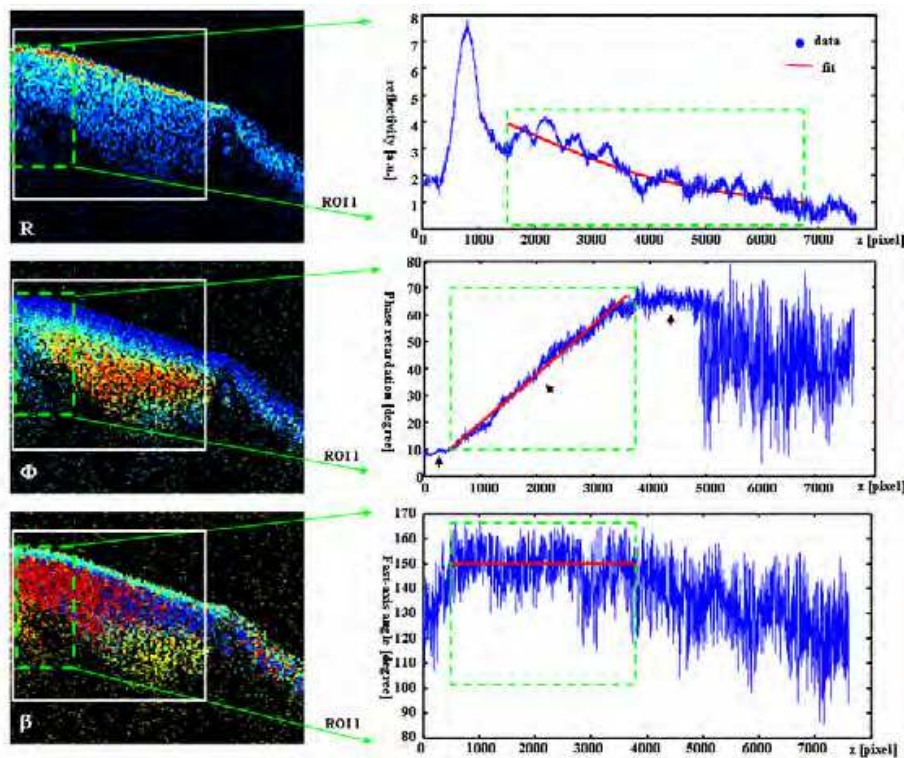


Fig. 7. Procedure of the PS-OCT extraction algorithm.

$k(k-1)$ , the number of comparisons. A Spearman's  $\rho$  correlation test was also used to evaluate whether these four properties have correlations with each other.

Finally, multinomial logistic regressions were used to generate a predictive model based on a linear combination of weights ( $X_{r\rho}$ ) of optical properties ( $\rho$  = scattering coefficient, effective anisotropy factor, birefringence, and fast-axis angle) as shown in this equation:

$$\text{logit}\left[\frac{OR(\text{diseased vessel type})}{OR(\text{Normal vessel})}\right] = A_r + \sum B_{r\rho} X_{r\rho} \quad (7)$$

Here OR = Odds Ratio,  $r = C/N, F/N, L/N$ ,  $A_r$  is a constant, and  $B_{r\rho}$  is an adjustable coefficient for each optical property. This model was used to classify the artery specimens into four diagnostic classes. The accuracy of this model for plaque characterization was evaluated using receiver operating characteristic (ROC) analysis (Metz, 1978).

Figures 3–6, given in previous pages, show illustrative PS-OCT images with the corresponding histopathology of normal, lipid, fibroatheroma, and fibrocalcific plaques. Altogether, 30 aortic specimens and therefore 135 ROIs from each region across totally R,  $\Phi$ , and  $\beta$  images were collected. The extracted data,  $\mu_s$ ,  $g_{eff}$ ,  $\Delta n$ , and  $\beta$ , are summarized in Fig. 8, where each box shows the median, 25th and 75th percentiles, and the extreme values within a category. Open circles and stars indicate outlier data.

Kruskal-Wallis statistics shows that  $\mu_s$  ( $p = 0.022$ ),  $\Delta n$  ( $p < 0.001$ ), and  $\beta$  ( $p < 0.001$ ) have significant differences in normal vessels and three types of atherosclerotic vessels, by measuring how much the ranks of the four groups differ from the mean rank of all groups. The  $g_{eff}$  value does not show any significant difference ( $p = 0.104$ ). From the multiple comparison test, we found that F to C shows significant difference in  $\mu_s$ ;  $\Delta n$  between C and

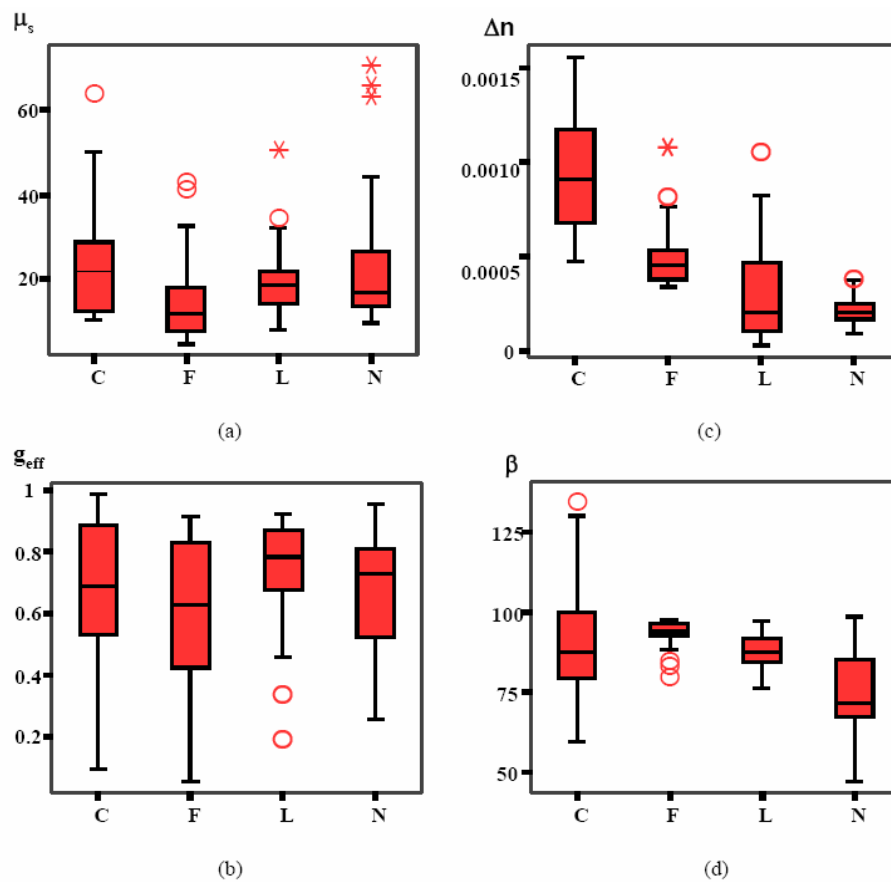


Fig. 8. Distributions of  $\mu_s$ ,  $g_{eff}$ ,  $\Delta n$ , and  $\beta$  in normal vascular intima (N), lipid laden (L), fibrous (F), and fibrocalcific (C) plaques.

N, F and N, L and C, and L and F has significant differences; and  $\beta$  between C and N, F and N, L and N, and L and F has significant differences.

Spearman's  $\rho$  correlation test shows that only  $g_{eff}$  correlates with the scattering coefficient ( $r = -0.584$ ,  $p = 0.003$ ) in fibrocalcific plaque, while this value correlates with the birefringence value ( $r = -0.563$ ,  $p = 0.008$ ) in fibrous lesions. Finally, three regression models, Equations (8)-(10), were used to predict the odds ratio of C to N, F to N, and L to N, respectively.

$$\text{logit} \left[ \frac{OR(\text{type} = C)}{OR(\text{type} = N)} \right] = -19.182 + 0.044X_{\mu_s} + 0.119X_{\Delta n} + 0.141X_{\beta} \quad (8)$$

$$\text{logit} \left[ \frac{OR(\text{type} = F)}{OR(\text{type} = N)} \right] = -19.377 - 0.047X_{\mu_s} + 0.068X_{\Delta n} + 0.201X_{\beta} \quad (9)$$

$$\text{logit} \left[ \frac{OR(\text{type} = L)}{OR(\text{type} = N)} \right] = -9.746 - 0.008X_{\mu_s} + 0.028X_{\Delta n} + 0.113X_{\beta} \quad (10)$$

The prediction results are given in Table 1. This method identified that 17 of 23 lesions are fibrocalcific and that 105 of 112 lesions are not fibrocalcific. In the case of fibrous plaque, 7 of 21 lesions were identified as fibrous and 110 of 114 as not fibrous lesions. Finally, the method identified 33 of 48 lesions as lipid regions and 55 of 87 as not lipid regions. The

constructed regression model achieved 90%, 87%, and 65% prediction accuracy for C, F, and L, respectively.

Classification				
Histology observed	Model predicted			
	N	C	F	L
N	27	0	0	16
C	1	17	2	3
F	0	1	7	13
L	7	6	2	33

Table 1. Plaque characterization by quantitative PS-OCT and histology

Our preliminary data indicated that more than 80% normal arterial samples had  $\mu_s$  value between 10 and 39  $\text{mm}^{-1}$  and have significant differences from other different types of plaques ( $p < 0.05$ ); this is consistent with the results obtained by Levitz (Levitz et al., 2004). From the multiple comparison tests, we also noticed that a significant difference in scattering property exists between fibrous and fibrocalcific plaques. These findings are consistent with the results obtained with qualitative image-based plaque characterization methods where fibrous and fibrocalcific plaques can be distinguished by the signal-rich and signal-poor regions respectively (Stamper et al., 2006; Yabushita et al., 2002). However, the effective anisotropy factor demonstrates no significant difference between normal and other atherosclerotic lesions ( $p = 0.104$ ), perhaps because  $g_{\text{eff}}$  of the fibrocalcific and fibrous lesions were correlated with  $\mu_s$  and  $\Delta n$ , respectively. In the case of the birefringence property of the vessel that has not been quantitatively analyzed previously, i.e.,  $\beta$  values, they were maximum in the most atherosclerotic lesion at over 70 degrees. Smaller  $\beta$  values were present in the best-fit areas of normal vascular intima. The  $\Delta n$  values were small and more concentrated in normal intima, but they demonstrated larger variations in the entire atherosclerotic lesion. The birefringence coefficient was larger in abundant thicker collagen fibers ( $\Delta n = 9.409 \times 10^{-4}$ ; bright yellow to orange color, constituting >60% of the left region of histology in Fig. 5c) than in thin collagen fibers ( $\Delta n = 5.386 \times 10^{-4}$ ; green color in right region of histology in Fig. 5c). Both  $\beta$  and  $\Delta n$  values have significant differences between the normal arterial vessel and other different types of plaques ( $p < 0.05$ ).

In this study, no attempt has been made to differentiate a necrotic core from a lipid pool. Since the signal from the necrotic cores may be too weak for reliable measurements, future studies based on histological stains that can differentiate the two are needed. It is also noteworthy that the  $\Phi$  and  $\beta$  signals are distributed in a slightly more random manner in the lipid lesion than in the normal vessel wall and fibrous and fibrocalcific plaques. This may be due to the polarization state of light that is to be randomized by multiple scattering in lipid-rich tissue, which reduces the accuracy of birefringence measurements. Alternatively, further modifications of these PS-OCT criteria, such as the addition of a threshold limit for the signal-poor region and incorporation of the standard deviation of the birefringence signal within one ROI, may be required to differentiate lipid lesions better.

## 5. Conclusion

Collagen fiber constitutes up to 60% of the total atherosclerotic plaque protein. Uncontrolled collagen accumulation leads to vascular stenosis, whereas excessive collagen breakdown

weakens plaques making them prone to rupture (Falk et al., 1995; Rekhter, 1999). Assessing the phase retardation change may be a method to quantify the collagen content in atherosclerotic lesions, and it may provide significant pathophysiological information that can influence clinical decision-making in patients with risk factors. Furthermore, computer-based quantitative analysis can automatically determine the plaque type; this will eliminate the training time for each reader and disparity between different diagnoses. The quantitative information on both arterial scattering and birefringence properties can also be integrated with the qualitative visual information provided by PS-OCT images, and this can support the facilitation of image-based plaque characterization methods. Our preliminary results present an important step in validating this new imaging modality and can provide a basis for the interpretation of PS-OCT images obtained from human specimens. However, an analysis from a considerably larger set of specimens as well as an analysis taking the effect of cluster data (i.e., specimens from the same person) into consideration will be required for developing a more suitable prediction model in the future. Moreover, it is likely that the combination of other functional modalities such as optical coherence elastography (Rogowska et al., 2004; 2006) or spectroscopic OCT (Morgner et al., 2000), which can provide additional indexes (such as cellular and molecular components and mechanical properties of arterial walls), will have a greater predictive value for constructing a risk-stratifying plaque characterization criterion that can be applied in future clinical utilities.

## 6. Acknowledgments

The authors thank Dr. N. K. Chou of the Department of Surgery of National Taiwan University Hospital for providing aortic tissues and Prof. J. J. Shyu of the Department of Veterinary Medicine of National Taiwan University for histology examinations. This research was supported by the National Science Council of Taiwan.

## 7. References

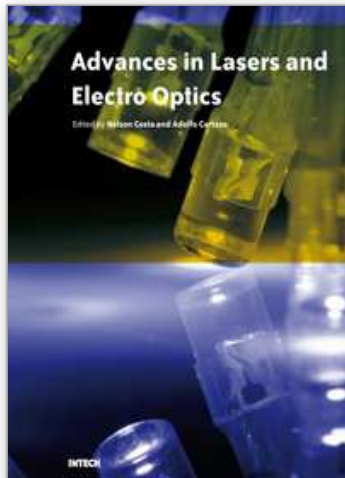
- Arroyo, L. H. & Lee, R. T. (1999). Mechanisms of plaque rupture: mechanical and biologic interactions. *Cardiovascular Research*, Vol. 41, No. 2, (369-375), ISSN 0008-6363
- Bouma, B. E.; Tearney, G. J.; Yabushita, H.; Shishkov, M.; Kauffman, C. R.; DeJoseph Gauthier, D.; MacNeill, B. D.; Houser, S. L.; Aretz, H. T.; Halpern, E. F. & Jang, I. K. (2003). Evaluation of intracoronary stenting by intravascular optical coherence tomography. *Heart*, Vol. 89, (317-321), ISSN 1355-6037
- Brezinski, M. E.; Tearney, G. J.; Bouma, B. E.; Izatt, J. A.; Hee, M. R.; Swanson, E. A.; Southern, J. F. & Fujimoto, J. G. (1996). Optical coherence tomography for optical biopsy: properties and demonstration of vascular pathology. *Circulation*, Vol. 93, (1206-1213), ISSN 0009-7322
- Brezinski, M. E.; Tearney, G. J.; Weissman, N. J.; Boppart, S. A.; Bouma, B. E.; Hee, M. R.; Weyman, A. E.; Swanson, E. A.; Southern, J. F. & Fujimoto, J. G. (1997). Assessing atherosclerotic plaque morphology: comparison of optical coherence tomography and high frequency intravascular ultrasound. *Heart*, Vol. 77, (397-403), ISSN 1355-6037
- de Boer, J. F.; Milner, T. E.; van Gemert, M. J. C. & Nelson, J. S. (1997). Two-dimensional birefringence imaging in biological tissue by polarization-sensitive optical coherence tomography. *Opt. Lett.*, Vol. 22, (934-936), ISSN 0146-9592

- Falk, E.; Shah, P. K. & Fuster, V. (1995) Coronary plaque disruption. *Circulation*, Vol. 110, (657-671), ISSN 0009-7322
- Fujimoto, J. G.; Bresinski, M. E.; Tearney, G. J.; Boppart, S. A.; Bouma, B. E.; Hee, M. R.; Southern, J. F. & Swanson, E. A. (1995). Optical biopsy and imaging using optical coherence tomography. *Nature Medicine*, Vol. 1, (970-972), ISSN 1078-8956
- Giattina, S. D.; Courtney, B. K.; Herz, P. R.; Harman, M.; Shortkroff, S.; Stamper, D. L.; Liu, B.; Fujimoto, J. G.; Brezinski, M. E. (2006). Assessment of coronary plaque collagen with polarization sensitive optical coherence tomography (PS-OCT). *Int J Cardiol*, Vol. 107, (400-409), ISSN 0167-5273
- Guo, S.; Zhang, J.; Wang, L.; Nelson, J. S. & Chen, Z. (2004). Depth-resolved birefringence and differential optical axis orientation measurements with fiber-based polarization-sensitive optical coherence tomography. *Opt. Lett.*, Vol. 17, (2025-2027), ISSN 0146-9592
- Hitzenberger, C. K.; Gotzinger, E.; Sticker, M.; Pircher, M. & Fercher, A. F. (2001). Measurement and imaging of birefringence and optic axis orientation by phase resolved polarization sensitive optical coherence tomography. *Opt. Express*, Vol. 9, (780-790), ISSN 1094-4087
- Huang, D.; Swanson, E. A.; Lin, C. P.; Schuman, J. S.; Stinson, W. G.; Chang, W.; Hee, M. R.; Flotte, T.; Gregory, K.; Pufialito, C. A. & Fujimoto, J. G. (1991). Optical coherence tomography. *Science*, Vol. 254, (1178-1181), ISSN 0036-8075
- Jang, I. K.; Bouma, B. E.; Kang, D. H.; Park, S. J.; Park, S. W.; Seung, K. B.; Choi, K. B.; Shishkov, M.; Schlendorf, K.; Pomerantsev, E.; Houser, S. L.; Aretz, H. T. & Tearney, G. J. (2002). Visualization of coronary atherosclerotic plaques in patients using optical coherence tomography: comparison with intravascular ultrasound. *J. Am. Coll. Cardiol.*, Vol. 39, (604-609), ISSN 0735-1097
- Kortum R. R. & Muraca, E. S. (1996). Quantitative optical spectroscopy for tissue diagnosis. *Ann. Rev. Phys. Chem.*, Vol. 47, (555-606), ISSN 0066-426X
- Kuo, W. C.; Shyu, J. J.; Chou, N. K.; Lai, C. M.; Huang, H. C.; Chou, C.; & Jan, G. J. (2004). Imaging of Human Aortic Atherosclerotic plaques by Polarization-Sensitive Optical Coherence Tomography, *Proceedings of IEEE Conference on Engineering in Medicine and Biology*, pp. 1111-1114, ISBN 0879425598, San Francisco, Aug 2004, EMBS, CA
- Kuo, W. C.; Shyu, J. J.; Chou, N. K.; Lai, C. M.; Tien, E. K.; Huang, H. J.; Chou, C. & Jan, G. J. (2005). Correlation of collagen synthesis with polarization-sensitive optical coherence tomography imaging of in vitro human atherosclerosis, *Proceedings of SPIE 5690*, pp. 563-571, ISBN 9780819456649, San Jose, January 2005, SPIE, CA.
- Kuo, W. C.; Chou, N. K.; Chou, C.; Lai, C. M.; Huang, H. J. & Shyu, J. J. (2007). Polarization-sensitive optical coherence tomography for imaging human atherosclerosis. *Appl. Opt.*, Vol. 46, (2520-2527), ISSN 0003-6935
- Kuo, W. C.; Hsiung, M. W. & Yang, P. N. (2007). Extracting quantitative optical properties of human vessel from PS-OCT images. *Journal of Medical and Biological Engineering*, Vol. 27, (191-197), ISSN 1609-0985
- Kuo, W. C.; Hsiung, M. W.; Shyu, J. J.; Chou, N. K. & Yang, P. N. (2008). Quantitative analysis on optical properties of human atherosclerosis by using polarization-sensitive optical coherence tomography, *Proceedings of SPIE 6842*, pp. 684223-1~684223-9, ISBN 9780819470171, San Jose, January 2008, SPIE, CA.

- Kuo, W. C.; Hsiung, M. W.; Shyu, J. J.; Chou, N. K. & Yang, P. N. (2008). Assessment of arterial characteristics in human atherosclerosis by extracting optical properties from polarization-sensitive optical coherence tomography. *Opt. Express*, Vol. 16, (8117-8125), ISSN 1094-4087
- Levitz, D.; Thrane, L.; Frosz, M. H.; Andersen, P. E.; Andersen, C. B.; Valanciunaite, J.; Swartling, J.; Andersson-Engels S. & Hansen, P. R. (2004). Determination of optical properties of highly-scattering media in optical coherence tomography. *Opt. Express*, Vol. 12, (249-259), ISSN 1094-4087
- Metz, C. E. (1978). Basic principles of ROC analysis. *Seminars in Nuclear Medicine*, Vol. 8, (283-298), ISSN 0001-2998
- Morgner, U.; Drexler, W.; Kartner, F. X.; Li, X. D.; Pitris, C.; Ippen, E. P. & Fujimoto, J. G. (2000). Spectroscopic optical coherence tomography. *Opt. Lett.*, Vol. 25, No. 2, (111-113), ISSN 0146-9592
- Nadkarni, S. K.; Pierce, M. C.; Park, B. H.; de Boer, J. F.; Whittaker, P.; Bouma, B. E.; Bressner, J. E.; Halpern, E.; Houser, S. L.; & Tearney, G. J. (2007). Measurement of collagen and smooth muscle cell content in atherosclerotic plaques using polarization sensitive optical coherence tomography. *J. Am. Coll. Cardiol.*, Vol. 49, (1474-1481), ISSN 0735-1097
- Park, B. H.; Pierce, M. C.; Cense, B.; Yun, S. H.; Mujat, M.; Tearney, G. J.; Bouma, B. E. & de Boer, J. F. (2005). Realtime fiber-based multi-functional spectral-domain optical coherence tomography at 1.3 mm. *Opt. Express*, Vol. 13, (3931-3944), ISSN 1094-4087
- Park, B. H.; Pierce, M. C.; Cense, B. & de Boer, J. F. (2004). Jones matrix analysis for a polarization-sensitive optical coherence tomography system using fiber-optic components. *Opt. Lett.*, Vol. 21, (2512-2514), ISSN 0146-9592
- Park, B. H.; Saxer, C.; Srinivas, S. M.; Nelson, J. S. & de Boer, J. F. (2001). In vivo burn depth determination by high-speed fiber-based polarization sensitive optical coherence tomography. *J. Biomed. Opt.*, Vol. 6, No. 4, (474-479), ISSN 1083-3668
- Pasterkamp, G.; Falk, E.; Woutman, J. & Borst, C. (2000). Techniques characterizing the coronary atherosclerotic plaque: Influence on clinical decision making. *J. Am. Coll. Cardiol.*, Vol. 36, (13-21), ISSN 0735-1097
- Peters, R. J. G.; Kok, W. E. M.; Havenith, M. G.; Rijsterborgh, H. & vanderWal, A. C. (1994). Histopathologic validation of intracoronary ultrasound imaging. *J. Am. Soc. Echocardiography*, Vol. 7, (230-241), ISSN 0894-7317
- Rekhter, M. D. (1999). Collagen synthesis in atherosclerosis: too much and not enough. *Cardiovascular Research*, Vol. 41, (376-384), ISSN 0008-6363
- Rogowska, J.; Patel, N. A.; Fujimoto, J. G. & Brezinski, M. E. (2004). Optical coherence tomographic elastography technique for measuring deformation and strain of atherosclerotic tissues. *Heart*, Vol. 90, No. 5, (556-562), ISSN 1355-6037
- Rogowska, J.; Patel, N. A.; Plummer, S. & Brezinski, M. E. (2006). Quantitative optical coherence tomographic elastography: method for assessing arterial mechanical properties. *Br. J. Radiol.*, Vol. 79, No. 945, (707-711), ISSN 1748-880X
- Saxer, C. E.; de Boer, J. F.; Park, B. H.; Shao, Y.; Chen, Z. & Nelson, J. S. (2000). High-speed fiber-based polarization-sensitive optical coherence tomography of in vivo human skin. *Opt. Lett.*, Vol. 18, (1355-1357), ISSN 0146-9592

- Shah, P. K. (2003). Mechanisms of plaque vulnerability and rupture. *J. Am. Coll. Cardiol.*, Vol. 41, No. 4, (15S-22S), ISSN 0735-1097
- Stamper, D.; Weissman, N. J.; Brezinski, M. (2006). Plaque characterization with optical coherence tomography. *J. Am. Coll. Cardiol.*, Vol. 47, (C69-C79), ISSN 0735-1097
- Tearney, G. J.; Jang, I-K & Bouma, B. E. (2006). Optical coherence tomography for imaging the vulnerable plaque. *J. Biomed. Opt.*, Vol. 11, No. 2, (021002), ISSN 1083-3668
- Tearney, G. J.; Yabushita, H.; Houser, S. L.; Aretz, H. T.; Janf, I. K.; Schlendorf, K. H.; Kauffman, C. R.; Shishkov, M.; Halpern, E. F. & Bouma, B. E. (2003). Quantification of macrophage content in atherosclerotic plaques by optical coherence tomography. *Circulation*, Vol. 107, (113-119), ISSN 0009-7322
- Thrane, L.; Yura, H. T. & Andersen, P. E. (2000). Analysis of optical coherence tomography systems based on the extended Huygens-Fresnel principle. *J. Opt. Soc. Am. A*, Vol. 17, (484-490), ISSN 1464-4258
- Villard, J. W.; Feldman, M. D.; Kim, J.; Milner, T. E. & Freeman, G. L. (2002). Use of a Blood Substitute to determine instantaneous murine right ventricular thickening with optical coherence tomography. *Circulation*, Vol. 105, (1843-1849), ISSN 0009-7322
- Yabushita, H.; Bouma, B. E.; Houser, S. L.; Aretz, H. T.; Jang, I. K.; Schlendorf, K. H.; Kauffman, C. R.; Shishkov, M.; Kang, D. H.; Halpern, E. F. & Tearney, G. J. (2002). Characterization of human atherosclerosis by optical coherence tomography. *Circulation*, Vol. 106, (1640-1645), ISSN 0009-7322
- Yamanari, M.; Makita, S.; Madjarova, V. D.; Yatagai, T. & Yasuno, Y. (2006). Fiber-based polarization-sensitive Fourier domain optical coherence tomography using B-scan-oriented polarization modulation method. *Opt. Express*, Vol. 14, (6502-6515), ISSN 1094-4087
- Zhang, J.; Jung, W.; Nelson, J. S. & Chen, Z. (2004). Full range polarization-sensitive Fourier domain optical coherence tomography. *Opt. Express*, Vol. 12, (6033-6039), ISSN 1094-4087

IntechOpen



## **Advances in Lasers and Electro Optics**

Edited by Nelson Costa and Adolfo Cartaxo

ISBN 978-953-307-088-9

Hard cover, 838 pages

**Publisher** InTech

**Published online** 01, April, 2010

**Published in print edition** April, 2010

Lasers and electro-optics is a field of research leading to constant breakthroughs. Indeed, tremendous advances have occurred in optical components and systems since the invention of laser in the late 50s, with applications in almost every imaginable field of science including control, astronomy, medicine, communications, measurements, etc. If we focus on lasers, for example, we find applications in quite different areas. We find lasers, for instance, in industry, emitting power level of several tens of kilowatts for welding and cutting; in medical applications, emitting power levels from few milliwatt to tens of Watt for various types of surgeries; and in optical fibre telecommunication systems, emitting power levels of the order of one milliwatt. This book is divided in four sections. The book presents several physical effects and properties of materials used in lasers and electro-optics in the first chapter and, in the three remaining chapters, applications of lasers and electro-optics in three different areas are presented.

### **How to reference**

In order to correctly reference this scholarly work, feel free to copy and paste the following:

Wen-Chuan Kuo (2010). Polarization-Sensitive Optical Coherence Tomography in Cardiology, *Advances in Lasers and Electro Optics*, Nelson Costa and Adolfo Cartaxo (Ed.), ISBN: 978-953-307-088-9, InTech, Available from: <http://www.intechopen.com/books/advances-in-lasers-and-electro-optics/polarization-sensitive-optical-coherence-tomography-in-cardiology>

**INTECH**  
open science | open minds

### **InTech Europe**

University Campus STeP Ri  
Slavka Krautzeka 83/A  
51000 Rijeka, Croatia  
Phone: +385 (51) 770 447  
Fax: +385 (51) 686 166  
[www.intechopen.com](http://www.intechopen.com)

### **InTech China**

Unit 405, Office Block, Hotel Equatorial Shanghai  
No.65, Yan An Road (West), Shanghai, 200040, China  
中国上海市延安西路65号上海国际贵都大饭店办公楼405单元  
Phone: +86-21-62489820  
Fax: +86-21-62489821

© 2010 The Author(s). Licensee IntechOpen. This chapter is distributed under the terms of the [Creative Commons Attribution-NonCommercial-ShareAlike-3.0 License](#), which permits use, distribution and reproduction for non-commercial purposes, provided the original is properly cited and derivative works building on this content are distributed under the same license.

IntechOpen

IntechOpen